JACS
JOURNAL OF THE AMERICAN CHEMICAL SOCIETY
Article
pubs.acs.org/JACS

Vacancy Associates Promoting Solar-Driven Photocatalytic Activity of Ultrathin Bismuth Oxychloride Nanosheets

Meili Guan,[†,§] Chong Xiao,[†,§] Jie Zhang,[‡] Shaojuan Fan,[‡] Ran An,[‡] Qingmei Cheng,[†] Junfeng Xie,[†] Min Zhou,[⊥] Bangjiao Ye,[‡] and Yi Xie*[,†]

[†]Hefei National Laboratory for Physical Sciences at the Microscale, [‡]State Key Laboratory of Particle Detection and Electronics, University of Science & Technology of China, Hefei, Anhui, 230026, P. R. China

[⊥]Institute of Physics & IMN MacroNano, Ilmenau University of Technology, 98693 Ilmenau, Germany

Supporting Information

ABSTRACT: Crystal facet engineering of semiconductors is of growing interest and an important strategy for fine-tuning solar-driven photocatalytic activity. However, the primary factor in the exposed active facets that determines the photocatalytic property is still elusive. Herein, we have experimentally achieved high solar photocatalytic activity in ultrathin BiOCl nanosheets with almost fully exposed active {001} facets and provide some new and deep-seated insights into how the defects in the exposed active facets affect the solar-driven photocatalytic property. As the thickness of the nanosheets reduces to atomic scale, the predominant defects change from isolated defects V'''_{Bi} to triple vacancy associates $V'''_{Bi}V^{\bullet\bullet}_{O}V'''_{Bi}$, which is unambiguously confirmed by the positron annihilation spectra. By virtue of the synergic advantages of enhanced adsorption capability, effective separation of electron−hole pairs and more reductive photoexcited electrons benefited from the $V'''_{Bi}V^{\bullet\bullet}_{O}V'''_{Bi}$ vacancy associates, the ultrathin BiOCl nanosheets show significantly promoted solar-driven photocatalytic activity, even with extremely low photocatalyst loading. The finding of the existence of distinct defects (different from those in bulks) in ultrathin nanosheets undoubtedly leads to new possibilities for photocatalyst design using quasi-two-dimensional materials with high solar-driven photocatalytic activity.

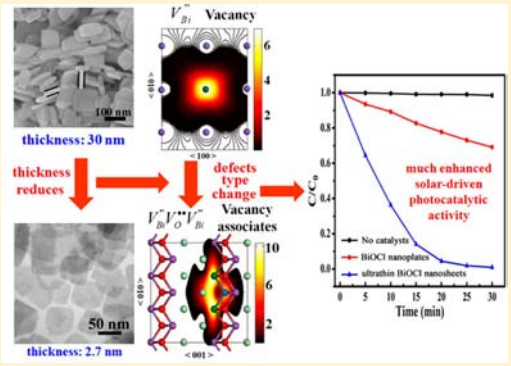

INTRODUCTION

Since the discovery of photocatalytic splitting of water on a TiO_2 electrode in 1972,[1] the efficient utilization of solar energy for photocatalytic processes underlying environment decontamination has been attracting massive research interest due to the increasing consciousness of the adverse impacts of industrialization on our environment.[2−4] During the past decades, various strategies, such as doping,[5−7] semiconductor recombination,[8,9] photosensitization,[10] deposition of noble metals[11,12] and so on, have been developed for the improvement of degradation efficiency under solar irradiation. Stimulated by the strong influence of crystal facets' characteristics, such as atomic arrangement, electronic structure, and defects, on the activity of photocatalysts, great interest has emerged in tuning the crystal facets of photocatalysts to optimize solar-driven photocatalytic reactivity.[13,14] As a result, facet engineering fully exposed with reactive facets is an exciting direction for developing highly active new photocatalysts. However, understanding of the mechanism of facet-dependent solar-driven photocatalytic properties still remains elusive.

Very recently, quasi-two-dimensional materials have attracted intensive attention because of their potential applications in optoelectronics,[15] energy storage,[16,17] catalysts,[18] and so on, which benefit from their high specific surface areas and large fraction of uncoordinated surface atoms with respect to the corresponding bulks. Furthermore, the exposed atoms on the surface of quasi-two-dimensional materials can easily escape from a lattice to form vacancies, which should affect the physical and chemical properties to a large extent. As a result, most efforts have been put into the exfoliated monolayers or synthesized ultrathin nanosheets from layered materials to explore their full potential.

As a novel layered ternary oxide semiconductor, bismuth oxyhalides (BiOX, X = Cl, Br, and I) have recently drawn much attention for their excellent photocatalytic performance,[19−21] comparable to or even better than that of anatase TiO_2, which benefits from their open crystalline structure. Bismuth oxyhalides have a layered structure (Figure 1) consisting of $[Bi_2O_2]^{2+}$ layers sandwiched between two slabs of halogen ions. In particular, recent works have demonstrated that BiOX nanoplates exposed with {001} facets exhibit excellent photoactivity, but understanding is still elusive, and the high oxygen vacancy density in {001} facets is usually deemed responsible for the enhanced photoactivity.[19] The typical layered structure of BiOCl with the stacking of $[Bi_2O_2]^{2+}$ layers along with z axis enables the possibility for synthesis of ultrathin nanosheets and even monolayered sheets with the

Received: March 24, 2013
Published: June 19, 2013

dx.doi.org/10.1021/ja402956f | J. Am. Chem. Soc. 2013, 135, 10411−10417

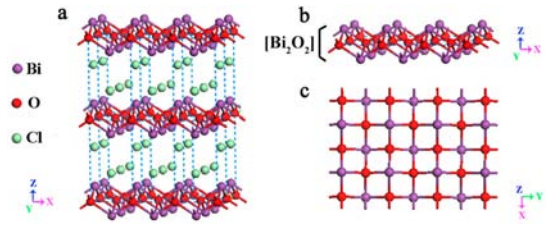

Figure 1. Schematic representation of the crystal structure of BiOCl. (a) Three-dimensional projection. (b, c) $[Bi_2O_2]^{2+}$ layers along with the [010] and [001] direction, respectively

inevitably improved percentage of exposed {001} planes, which usually contribute to the high efficiency of photocatalysts. In this regard, the BiOCl ultrathin nanosheet is a noteworthy model material for in-depth and comprehensive understanding of facet-dependent photocatalytic property.

Herein, we experimentally achieved high solar photocatalytic activity in ultrathin BiOCl nanosheets with almost fully exposed active {001} facets. As the thickness of the nanosheets reduces to atomic scale, the predominant defects change from isolated defects V'''_{Bi} to triple vacancy associates $V'''_{Bi}V^{\bullet\bullet}_{O}V'''_{Bi}$, which is unambiguously confirmed by the positron annihilation spectra. This $V'''_{Bi}V^{\bullet\bullet}_{O}V'''_{Bi}$ vacancy associate not only enhanced the adsorption capability but also effectively separated the electron−hole pairs in the ultrathin BiOCl nanosheets, which resulted in significantly promoted solar-driven photocatalytic activity with extremely low photocatalyst loading.

EXPERIMENTAL SECTION

Materials. All chemicals were of analytical grade purity, obtained from Sinopharm Chemical Reagent Co., Ltd., and used as received without further purification.

Synthesis of Ultrathin BiOCl Nanosheets. The ultrathin BiOCl nanosheets were synthesized using a modification of the method proposed by Xiong et al.[22] In a typical synthesis, 0.486 g of $Bi(NO_3)_3{\cdot}5H_2O$ and 0.400 g of PVP were dissolved in 25 mL of 0.1 M mannitol solution with vigorous stirring for 10 min. Then, 5 mL of saturated NaCl solution was slowly added into the above mixture, yielding a uniform white suspension. After another 10 min of agitation, the mixture was transferred into a Teflon-lined stainless steel autoclave of 45 mL capacity, which was heated at a temperature of 160 °C for 3 h and then cooled to room temperature naturally. The resulting solid powder was collected by centrifugation and washed with deionized water several times to remove residual ions. The final products were then dried at 60 °C for 4 h for further characterization.

Synthesis of BiOCl Nanoplates. For the BiOCl nanoplates, 0.486 g of $Bi(NO_3)_3{\cdot}5H_2O$ was dissolved in 25 mL of 0.1 M mannitol solution with vigorous stirring for 10 min. Then, 5 mL of saturated NaCl solution was slowly added into the above mixture, yielding a uniform white suspension. After another 10 min of agitation, the mixture was transferred into a Teflon-lined stainless steel autoclave of 45 mL capacity, which was heated at a temperature of 160 °C for 3 h and then cooled to room temperature naturally. The resulting solid powder was collected by centrifugation and washed with deionized water several times to remove residual ions. The final products were then dried at 60 °C for 4 h for further characterization.

Characterization. Powder X-ray diffraction patterns (XRD) were recorded on Japan Rigaku D/max-rA equipped with graphite monochromatized high-intensity Cu Kα radiation (λ = 1.54178 Å). The field-emission scanning electron microscopy (FESEM) images were obtained by using a JEOL JSM-6700F scanning electron microscope. Tapping-mode atomic force microscopy (AFM) images were obtained on a DI Innova Multimode SPM platform. The transmission electron microscopy (TEM) images were taken on a H-7650 (Hitachi, Japan) operated at an acceleration voltage of 100 kV. High-resolution transmission electron microscopy (HRTEM) and the corresponding electron diffraction (ED) analyses were carried out by using a JEOL-2010 TEM at an acceleration voltage of 200 kV. Room-temperature UV−vis absorption spectroscopy was conducted on a Perkin-Elmer Lambda 950 UV−vis−NIR spectrophotometer using an integrating-sphere accessory. X-ray photoelectron spectroscopy (XPS) valence spectra were acquired on an ESCALAB MKII X-ray photoelectron spectrometer with an excitation source of Mg Kα = 1253.6 eV.

Positron Annihilation Measurement. The positron lifetime experiments were carried out with a fast−slow coincidence ORTEC system with a time resolution of ~230 ps full width at half-maximum. A 5mCi source of ^{22}Na was sandwiched between two identical samples, and the total count was 1 million. Positron lifetime calculations were performed using the ATSUP method,[23] in which the electron density and the positron crystalline Coulomb potential are constructed by the non-self-consistent superposition of free atom electron density and Coulomb potential in the absence of the positron. Our calculations of the positron lifetime used the electron-positron enhancement factor due to Barbiellini et al.[24] described within the generalized gradient approximation. Positron lifetime calculations were performed for unrelaxed structure monovacancy defects and vacancy associates in BiOCl using 3 × 3 × 2 supercells.

Photocatalytic Measurement. Photocatalytic activities of the as-prepared products were evaluated by examining the photodegradation of Rhodamine B (RhB) under simulated solar irradiation from a 150 W Xe lamp (PLS-SXE300/300UV, Trusttech Co., Ltd. Beijing). For comparison, the UV and visible light photocatalytic activities were also evaluated with a 150 W high-pressure mercury lamp (λ = 365 nm) or a 150 W Xe lamp with a 420 nm cutoff filter as the UV or visible light source, respectively. Typically, 5 mg of catalyst was added into 100 mL of 10^{-5} M RhB aqueous solution. Before illumination, the suspension was placed in the dark under constant stirring for 120 min to reach adsorption/desorption equilibrium. Five milliliters of the suspension was withdrawn every 5 min under irradiation and centrifuged to remove the photocatalyst for UV−vis absorption spectrum measurements. The concentration of RhB was determined by monitoring its characteristic absorption at 554 nm.

RESULTS AND DISCUSSION

In this study, we first report the one-step selective synthesis of free-standing ultrathin BiOCl nanosheets with atomic thickness via a simple solvothermal method. The crystallinity and phase purity of the products were confirmed by XRD analysis. As shown in Figure 2a, the XRD pattern could be well indexed to the tetragonal phase of BiOCl with the lattice parameters of a = 0.3891 nm and c = 0.7369 nm (JCPDS No. 6-249). The enhanced relative intensity of the (001) peak clearly reveals a highly preferred (001) orientation in the nanosheets (Figure 2b). No characteristic peaks of any other phases and impurities are observed, indicating the high purity of the products.

The morphological feature of as-prepared ultrathin BiOCl nanosheets was characterized by TEM and is shown in Figure 2c. It is apparent that the particles are squarelike nanosheets with a size in the range of 50−100 nm. The HRTEM image (Figure 2d) exhibits good crystalline and clear lattice fringes projected along the [001] axis. The continuous lattice fringes with an interplanar lattice spacing of 0.275 nm and an angle of 90° match well with the (110) atomic planes of the tetragonal BiOCl. As depicted in Figure 2e, the corresponding selected-area electron diffraction (SAED) pattern displays a spot pattern, indicating the single-crystalline characteristic of the obtained nanosheets. The angle of adjacent spots labeled in the SAED pattern is 45°, which is identical to the theoretical value of the angle between the (110) and (200) planes of tetragonal

dx.doi.org/10.1021/ja402956f | J. Am. Chem. Soc. 2013, 135, 10411−10417

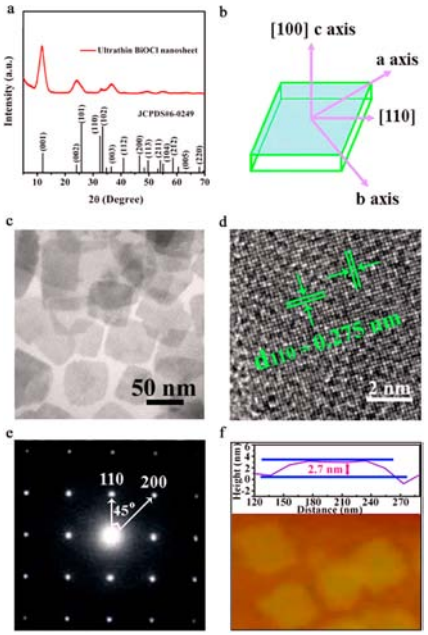

Figure 2. Characterizations of ultrathin BiOCl nanosheets. (a) XRD pattern; the black lines give the corresponding standard pattern of JCPDScard no. 6-0249. (b) Schematic illustration of the crystal orientation of the nanosheet. (c–e) TEM, HRTEM images and SAED pattern of the ultrathin BiOCl nanosheet. (f) Atomic force microscopic image with an average thickness of 2.7 nm.

BiOCl. It means that the set of diffraction spots can be indexed as the [001] zone axis, which agrees well with the XRD result.

More reliable information on the thickness of the ultrathin BiOCl nanosheets was obtained from the AFM image and the corresponding height profile was shown in Figure 2f. As can be seen, the thickness of these nanosheets is estimated to be ~2.7 nm. The lateral size of nanosheets measured by AFM is consistent with that from the TEM images. Considering that the *c* parameter of BiOCl is 7.37 Å, it can be deduced that each ultrathin BiOCl nanosheet with a 2.7 nm thickness consists of nearly 4 [Cl–Bi–O–Bi–Cl] units. As a comparison, the BiOCl nanoplates sample, with different thickness compared with ultrathin BiOCl nanosheets, was also prepared under similar synthesis conditions. The scanning electron microscopy image (Supporting Information Figure S1) shows that these BiOCl nanoplates are also squarelike in morphology, with a size of about 50–100 nm and thickness of about 30 nm. The results of HRTEM and SAED of the nanoplates are in accordance with those of the ultrathin nanosheets. On the basis of the above structural information, the percentage of highly reactive (001) facets in the ultrathin BiOCl nanosheets is estimated to be 95%, whereas the percentage is 62% in BiOCl nanoplates.

The photocatalytic degradation of organic dyes or toxic pollutants, which is of great significance in environmental pollutant treatment, represents a commonly used approach to characterize the activity of photocatalysts. The photocatalytic activity of ultrathin BiOCl nanosheets is evaluated under simulated solar irradiation using Rhodamine B (RhB) as a probe molecule in aqueous solution, and the relevant data for the BiOCl nanoplates sample is also given for comparison. In the absence of photocatalysts, decomposition of RhB is inappreciable within the test period, suggesting that photolysis of RhB is negligible. The characteristic absorbance at 554 nm of RhB in aqueous solution decreases more quickly with time of solar irradiation for ultrathin BiOCl nanosheets than for BiOCl nanoplates (Figure 3a and b). As seen in Figure 3c, the

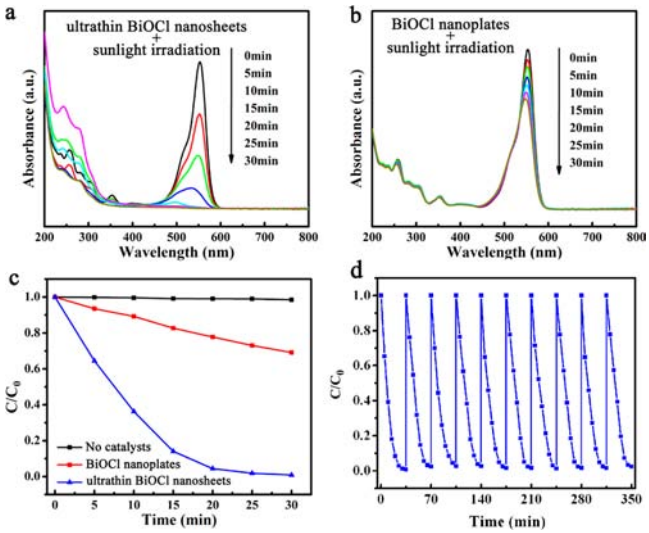

Figure 3. Photocatalytic activity of both the BiOCl nanoplates and ultrathin BiOCl nanosheets. (a–c) Comparison of photodecomposition of Rhodamine B with ultrathin BiOCl nanosheets and BiOCl nanoplates under the simulated solar irradiation. (d) Cycling curve of photocatalytic degradation of Rhodamine B for ultrathin BiOCl nanosheets with near fully exposed {001} facets.

decoloration rate of RhB in the presence of ultrathin BiOCl nanosheets reaches 98% after 20 min, but only less than 20% of RhB molecules are decomposed with nanoplates in the same period.

In addition, to confirm the stability of the high photocatalytic performance of the ultrathin BiOCl nanosheets, recycling experiments for the photodegradation of RhB were conducted. The result is shown in Figure 3d. The photodegradation rate remains constant over 10 consecutive cycles, indicating that the as-prepared photocatalyst is stable under UV–vis light irradiation, which is especially important for its application. It is worth noting that the excellent solar photocatalytic activity is obtained in the presence of very small amounts of photocatalysts (0.05 g/L), which suggests the striking potential of these ultrathin BiOCl nanosheets for practical technology application. Our results undoubtedly demonstrate that the ultrathin BiOCl nanosheets have superior solar photocatalytic activity compared with BiOCl nanoplates.

It is well-known that two photocatalytic pathways have been established for the degradation of dyes on semiconductors,[20,25,26] that is, direct semiconductor photoexcitation and indirect dye photosensitization, which responds differently to light of different wavelengths. To this end, the photocatalytic performance of both the ultrathin BiOCl nanosheets and BiOCl nanoplates was investigated under both UV and visible light irradiation. As seen in Figure 4a–e, the photocatalytic reactivity of ultrathin BiOCl nanosheets under both UV and visible light irradiation is much enhanced compared with that of BiOCl nanoplates. Because the band gap of BiOCl in our study is larger than 3.0 eV (see below), only UV light could be absorbed to activate the photocatalysts. Thus, our results undoubtedly indicate the enhancement of both direct semiconductor photoexcitation and indirect dye photosensitization in the ultrathin BiOCl nanosheets. As a result, by virtue of the synergic reinforcement of both direct semiconductor photo-

dx.doi.org/10.1021/ja402956f | J. Am. Chem. Soc. 2013, 135, 10411–10417

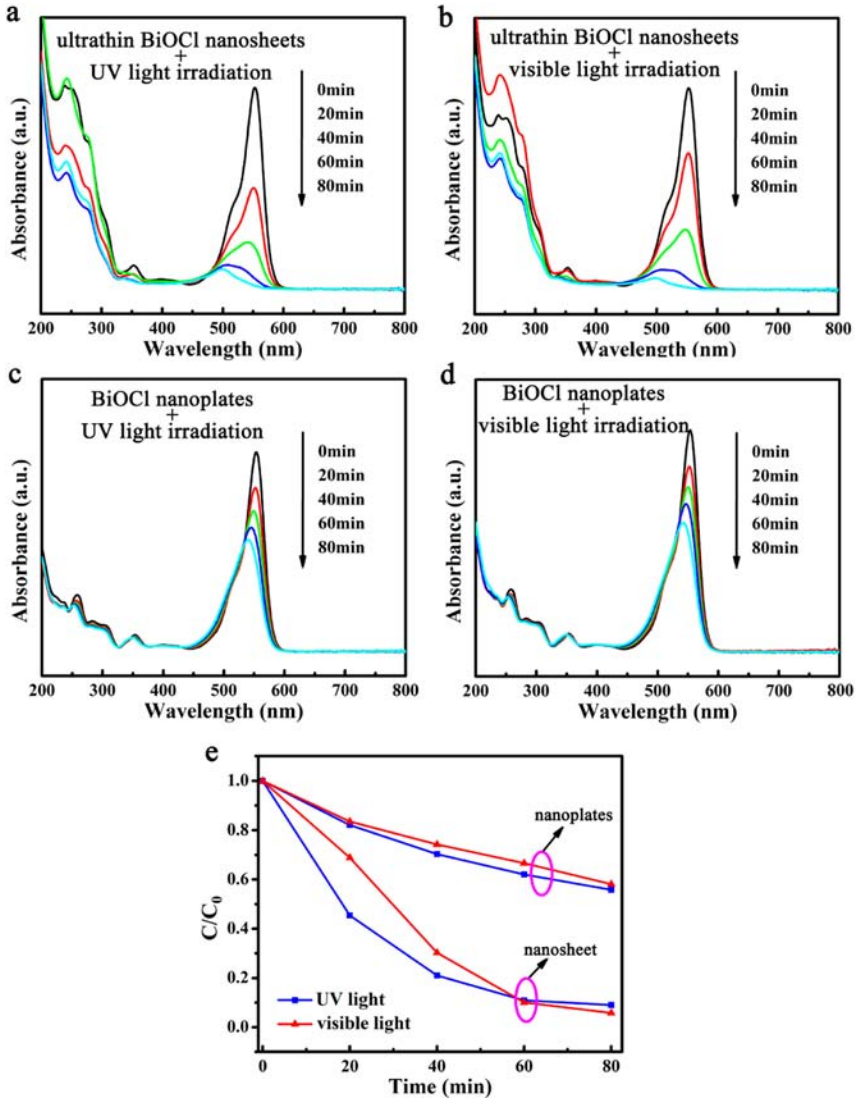

Figure 4. (a, b) Photodecomposition of Rhodamine B with ultrathin BiOCl nanosheets under UV and visible light irradiation, respectively. (c, d) Photodecomposition of Rhodamine B with BiOCl nanoplates under UV and visible light irradiation, respectively. (e) Comparison of photodecomposition of Rhodamine B vs time by ultrathin BiOCl nanosheets and BiOCl nanoplates under UV and visible light irradiation, respectively.

excitation and indirect dye photosensitization, the ultrathin BiOCl nanosheets show solar-driven photocatalytic performance superior to that of BiOCl nanoplates.

Although the high oxygen vacancy density on {001} facets is usually thought to be responsible for the enhanced photoactivity, it has not been verified.[19] In fact, the types and quantities of defects in the semiconductors strongly affect their properties. Therefore, both the identification and quantification of defects are necessary for in-depth and comprehensive understanding of facet-dependent photocatalytic properties. Positron annihilation spectrometry is a well established technique to study the defects in solids, and measuring the lifetime of the positron can give information about the type and relative concentration of defects/vacancies, even at the parts-per-million level.[27,28] The positron lifetime spectra of both BiOCl ultrathin nanosheets and BiOCl nanoplates yield four lifetime components (Figure 5a and Table 1).

The two longer components (τ_3, 550−590 ps and τ_4, 2.2−2.5 ns) are due to positron annihilation in the large defect clusters and the interface present in the material, respectively. According to the theoretically calculated lifetime of positrons (Table 2), the shortest one (τ_1, around 250 ps) observed in the experimental positron lifetime spectra could be attributed to positron annihilation as trapped at the single isolated bismuth vacancies (Figure 5b), whereas another component (τ_2, around 325 ps) could be assigned to Bi^{3+}−oxygen vacancy associates, $V_{Bi}'''V_O^{\bullet\bullet}V_{Bi}'''$ (Figure 5c). The relative intensity (Table 1) of the positron lifetime gives more information on the distribution of these defects, since the relative intensity can quantify the abundance of that defect with respect to some standard of the same material.[27] It is clear that triple Bi^{3+}−oxygen vacancy associates are predominant in ultrathin BiOCl nanosheets, but isolated bismuth vacancies are predominant in BiOCl nanoplates.

It is well-known that the surface atoms can escape from the lattice easier than the inner atoms. Taking into account the crystal structure of BiOCl, in the $[Bi_2O_2]^{2+}$ layers, the Bi atoms are exposed outside while the O atoms are buried inside (as seen in Figure 1b), which means that the Bi atoms should escape from the lattice more easily than the inner atoms,

dx.doi.org/10.1021/ja402956f | J. Am. Chem. Soc. 2013, 135, 10411−10417

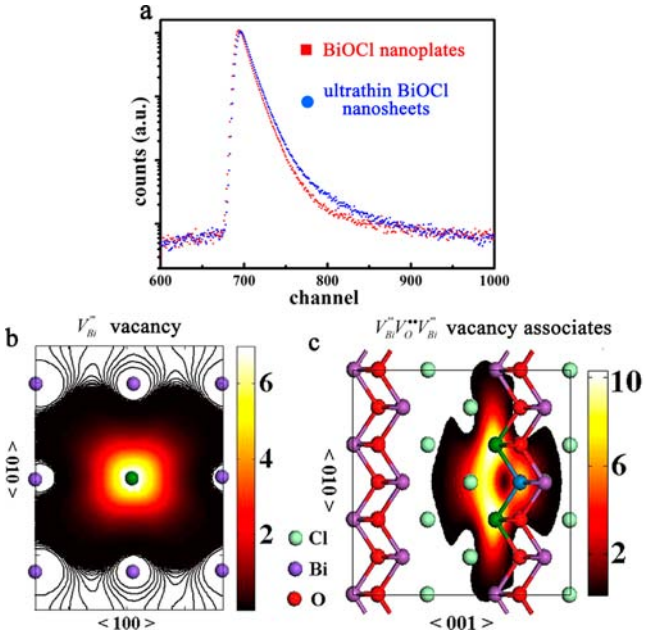

Figure 5. Positron annihilation spectroscopy of ultrathin BiOCl nanosheets and BiOCl nanoplates. (a) Positron lifetime spectrum of ultrathin BiOCl nanosheets and BiOCl nanoplates, respectively. (b, c) Schematic representations of trapped positrons of V'''_{Bi} defect and $V'''_{Bi}V^{\bullet\bullet}_{O}V'''_{Bi}$ vacancy associates, respectively.

resulting in the predominant defects of isolated Bi vacancy for the BiOCl nanoplates. When the thickness of BiOCl is reduced to atomic scale, it also becomes easier for the buried internal oxygen atoms to escape, making formation of the triple vacancy associates in the ultrathin BiOCl nanosheets easier. This result implies that the vacancy associates should be responsible for the enhanced photocatalytic activity in materials nearly fully exposed with {001} facets. This long-neglected aspect has not been discussed in previous reports.

As well-known, a prerequisite for the photosensitization pathway is the adsorption of dye molecules on the photocatalyst surface for the injection of photoexcited electrons into the conduction band (CB) of the semiconductor,[19,25,26] so the charge of photocatalyst surface and dye molecules is crucial for the adsorption. In our study, according to the positron annihilation results, the $V'''_{Bi}V^{\bullet\bullet}_{O}V'''_{Bi}$ vacancy associates are overwhelming defects with four negative charges in ultrathin BiOCl nanosheets. As a result, the (001) facets in ultrathin BiOCl nanosheets are more negatively charged than in BiOCl nanoplates, which favors the adsorption of positively charged RhB molecules. Figure 6a clearly shows the higher adsorption capability of ultrathin BiOCl nanosheets than BiOCl nanoplates.

To further validate the assumption that the more negatively charged (001) facets caused by the $V'''_{Bi}V^{\bullet\bullet}_{O}V'''_{Bi}$ vacancy associates are favorable for the adsorption of positively charged RhB molecules, another anionic dye, Methyl Orange (MO), was used as a target dye for comparison. Indeed, it is difficult for the anionic dye to be adsorbed on ultrathin BiOCl nanosheets. The viselike adsorbed dye molecules could more effectively inject their photoexcited electrons into the CB of the semiconductor, which then react with surface-adsorbed molecular oxygen to generate active species for pollutant degradation (Figure 6b). The detailed generation and transfer of photogenerated carriers in the indirect dye photosensitization pathways are shown in Supporting Information Figure S3. Thus, it is reasonable to believe that the ultrathin BiOCl nanosheets show higher photocatalytic activity than BiOCl nanoplates under visible light irradiation in our study.

Moreover, the change of defect type induced the enhanced visible light absorption (as seen in Figure 7a), which may contribute to the promotion of visible-light-driven photocatalytic performance. Thus, to confirm the leading role of indirect dye photosensitization on the enhanced visible-light-driven photodegradation of this color organics, we performed a parallel experiment of photodegradation of colorless organics (e.g. phenol) with the ultrathin BiOCl nanosheets under visible light irradiation. The results are shown in Figure S2 in the Supporting Information. As shown in Figure S2, in the absence of photocatalysts, decomposition of phenol and RhB under visible light irradiation is inappreciable within the test period, suggesting that photolysis of phenol and RhB is negligible. In the presence of ultrathin BiOCl nanosheets, the degradation of phenol under visible light irradiation becomes distinct. Because the phenol cannot absorb visible light, the indirect dye photosensitization degradation process cannot take place. Hence, the promoted photocatalytic performance in visible light region should be derived from the enhanced absorption of visible light by the ultrathin BiOCl nanosheet, which is, in fact, induced by the triple vacancy associates. However, compared with the degradation of RhB, the promotion of visible photocatalytic activity on the degradation of colorless organics is very limited. As seen in Supporting Information Figure S2, it is clear that the degradation rate of RhB is much more quick than that of colorless organics, so it is reasonably believed that the indirect dye photosensitization plays a crucial role in the degradation of dyes with ultrathin BiOCl nanosheets under visible light irradiation. Therefore, we can conclude that indirect dye photosensitization should play a leading role in the visible-light-driven photodegradation of color organics.

More importantly, it is well-known that the defect type should strongly affect the band structure of semiconductors, which further affects their photocatalytic activity. UV/vis absorption spectra (Figure 7a and b) reveal that the band gap of the ultrathin BiOCl nanosheets is ~3.00 eV, slightly smaller than that of BiOCl nanoplates (3.25 eV), which can be attributed to the existence of predominating $V'''_{Bi}V^{\bullet\bullet}_{O}V'''_{Bi}$ vacancy associates in the as-obtained ultrathin BiOCl nanosheets. The valence band (VB) of both BiOCl nanoplates and ultrathin BiOCl nanosheets is measured by XPS valence spectra, as shown in Figure 7c. The BiOCl nanoplates display a VB with the edge of the maximum energy at about 2.22 eV. That is to say, according to the optical absorption spectrum, the CB minimum would occur at about −1.03 eV. Meanwhile, for the ultrathin BiOCl nanosheets, the VB maximum energy up-shifts

Table 1. Positron Lifetime Parameters of Ultrathin BiOCl Nanosheets and BiOCl Nanoplates

sample	τ_1 (ps)	τ_2 (ps)	τ_3 (ps)	τ_4 (ns)	I_1 (%)	I_2 (%)	I_3 (%)	I_4 (%)
nanosheets	243.1	326.6	578.8	2.266	13.70	71.02	12.63	2.65
nanoplates	252.2	320.1	559.2	2.491	49.32	35.68	13.91	1.09

dx.doi.org/10.1021/ja402956f | J. Am. Chem. Soc. 2013, 135, 10411−10417

Table 2. Calculated Positron Lifetime Values of BiOCl

defect	bulk	$V_O^{\bullet\bullet}$	V_{Bi}'''	$V_O^{\bullet\bullet}V_O^{\bullet\bullet}$	$V_{Bi}'''V_{Bi}'''$	$V_{Bi}'''V_O^{\bullet\bullet}$	$V_O^{\bullet\bullet}V_{Bi}'''V_O^{\bullet\bullet}$	$V_{Bi}'''V_O^{\bullet\bullet}V_{Bi}'''$
lifetime (ps)	175	178	248	182	275	271	272	325

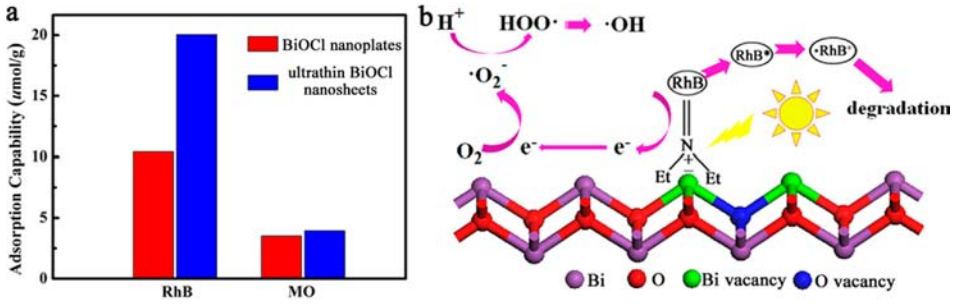

Figure 6. Adsorption and photosensitization of ultrathin BiOCl nanosheets and BiOCl nanoplates. (a) Adsorption amounts of RhB and MO over ultrathin BiOCl nanosheets and BiOCl nanoplates, respectively. (b) Schematic diagram illustrating photosenstization process under visible light irradiation.

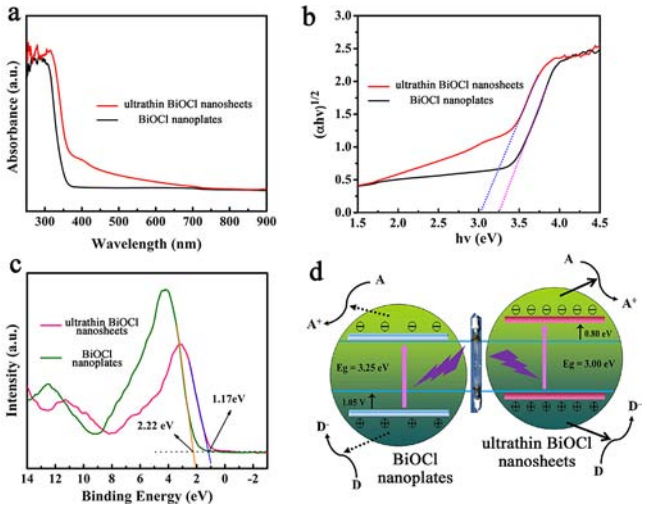

Figure 7. Band structure change between ultrathin BiOCl nanosheets and BiOCl nanoplates. (a) UV/vis absorption spectra of ultrathin BiOCl nanosheets and BiOCl nanoplates. (b) The bandgap value, estimated by a related curve of $(\alpha h\nu)^{1/2}$ versus photon energy plotted. (c) Valence-band XPS spectra of the ultrathin BiOCl nanosheets and BiOCl nanoplates. (d) Schematic illustration of the band structure of ultrathin BiOCl nanosheets and BiOCl nanoplates, the upshifting of valence band maximum, and conduction band minimum effectively separate the photoinduced electron−hole pairs in ultrathin BiOCl nanosheets.

by 1.05 to 1.17 eV compared with that of BiOCl nanoplates. Combined with the results of optical measurements, the CB minimum of ultrathin BiOCl nanosheets up-shifts by 0.8 eV and occurs at −1.83 eV compared to that of BiOCl nanoplates.

From the point of view of kinetic and thermodynamic requirements for direct semiconductor photoexcitation photocatalytic reactions, two features are worthy of noting:[29] the VB width and the CB minimum energy (Figure 7d). The raised VB width is beneficial for the separation of the charge carriers, since the VB width intrinsically controls the mobility of holes: the wider VB results in the higher mobility of holes generated, which leads to the better photo-oxidation of holes. On the other hand, the up-shifting of CB should play two crucial roles in the photocatalytic property: the elevation of the CB minimum not only makes the photogenerated electrons more negative to react with molecular oxygen to generate superoxide ions but also promotes the transfer of photoexcited electrons to reactants, resulting in the inhibition of the electron−hole recombination.[29] The detailed generation and transfer of photogenerated carriers in the direct semiconductor photoexcitation pathways are shown in the Supporting Information Figure S4. As a result, the ultrathin BiOCl nanosheets show more superior photocatalytic activity than BiOCl nanoplates.

CONCLUSION

In summary, we have for the first time demonstrated the momentous effect of vacancy associates in ultrathin nanosheets with fully exposed active facets on the photocatalytic activity. As an example, the insights gained from the experimental results in this study indicate that the $V_{Bi}'''V_O^{\bullet\bullet}V_{Bi}'''$ vacancy associates are predominant in the ultrathin BiOCl nanosheets, which is obviously different from the BiOCl nanoplates. These $V_{Bi}'''V_O^{\bullet\bullet}V_{Bi}'''$ vacancy associates not only make the (001) facets negatively charged for the enhanced adsorption of cationic dye molecules onto the photocatalysts, which facilitates the photosensitization process, but also narrow the band gap with both up-shifted valence band maximum and conduction band minimum, which effectively separates the photoinduced electron−hole pairs. By virtue of the synergetic promotion of both the dye photosensitization under visible light irradiation and direct semiconductor photoexcitation under UV light irradiation, the ultrathin BiOCl nanosheets show excellent solar photocatalytic activity, even with an extremely low photocatalysts loading. Our results provide some new insights for in-depth understanding of the facet-dependent photocatalytic property. This may open a new avenue for photocatalyst design with high solar-driven photocatalytic performance by engineering the intrinsic defects on the surface.

ASSOCIATED CONTENT

Supporting Information

Characterization of BiOCl nanoplates, detailed generation and transfer of photogenerated carriers both in indirect dye photosensitization and direct semiconductor photoexcitation pathways. This material is available free of charge via the Internet at http://pubs.acs.org.

AUTHOR INFORMATION

Corresponding Author

yxie@ustc.edu.cn

Author Contributions

[§]M.G. and C.X. contributed equally to this work.

Notes

The authors declare no competing financial interest.

ACKNOWLEDGMENTS

The authors thank the National Basic Research Program of China (2009CB939901), the Chinese Academy of Sciences (XDB01020300), and the National Natural Science Foundation of China (11079004, 11175171) for financial support.

REFERENCES

(1) Fujishima, A.; Honda, K. *Nature* **1972**, *238*, 37.
(2) Clasen, T.; Edmondson, P. *Int. J. Hyg. Environ. Health* **2006**, *209*, 173.
(3) Palmisano, G.; Augugliaro, V.; Pagliaro, M.; Palmisano, L. *Chem. Commun.* **2007**, *43*, 3425.
(4) Chen, C. C.; Ma, W. H.; Zhao, J. C. *Chem. Soc. Rev.* **2010**, *39*, 4206.
(5) Xiong, Z. G.; Zhao, X. S. *J. Am. Chem. Soc.* **2012**, *134*, 5754.
(6) Wang, J.; Tafen, D. N.; Lewis, J. P.; Hong, Z. L.; Manivannan, A.; Zhi, M. J.; Li, M.; Wu, N. Q. *J. Am. Chem. Soc.* **2009**, *131*, 12290.
(7) In, S.; Orlov, A.; Berg, R.; Garcia, F.; Pedrosa-Jimenez, S.; Tikhov, M. S.; Wright, D. S.; Lambert, R. M. *J. Am. Chem. Soc.* **2007**, *129*, 13790.
(8) Woan, K.; Pyrgiotakis, G.; Sigmund, W. *Adv. Mater.* **2009**, *21*, 2233.
(9) Buonsanti, R.; Grillo, V.; Carlino, E.; Giannini, C.; Gozzo, F.; Garcia.-Hernandez, M.; Garcia, M. A.; Cingolani, R.; Cozzoli, P. D. *J. Am. Chem. Soc.* **2010**, *132*, 2437.
(10) Pan, L.; Zou, J. J.; Zhang, X. W.; Wang, L. *J. Am. Chem. Soc.* **2011**, *133*, 10000.
(11) Teranishi, M.; Naya, S.; Tada, H. *J. Am. Chem. Soc.* **2010**, *132*, 7850.
(12) Su, R.; Tiruvalam, R.; He, Q.; Dimitratos, N.; Kesavan, L.; Hammond, C.; Lopez-Sanchez, J. A.; Bechstein, R.; Kiely, C. J.; Hutchings, G. J.; Besenbacher, F. *ACS Nano* **2012**, *6*, 6284.
(13) Liu, G.; Yu, J. C.; Lu, G. Q.; Cheng, H. M. *Chem. Commun.* **2011**, *47*, 6763.
(14) Kubacka, A.; Fernández-García, M.; Colón, G. *Chem. Rev.* **2012**, *112*, 1555.
(15) Radisavljevic, B.; Radenovic, A.; Brivio, J.; Giacometti, V.; Kis, A. *Nat. Nanotechnol.* **2011**, *6*, 147.
(16) Zhu, Y. W.; Murali, S. T.; Stoller, M. D.; Ganesh, K. J.; Cai, W. W.; Ferreira, P. J.; Pirkle, A.; Wallace, R. M.; Cychosz, K. A.; Thommes, M.; Su, D.; Stach, E. A.; Ruoff, R. S. *Science* **2011**, *332*, 1537.
(17) Feng, J.; Sun, X.; Wu, C.; Peng, L.; Lin, C.; Hu, S.; Yang, J.; Xie, Y. *J. Am. Chem. Soc.* **2011**, *133*, 17832.
(18) Sun, Y. F.; Sun, Z. H.; Gao, S.; Cheng, H.; Liu, Q. H.; Piao, J. Y.; Yao, T.; Wu, C. Z.; Hu, S. L.; Wei, S. Q.; Xie, Y. *Nat. Commun.* **2012**, *3*, 1057.
(19) Ye, L. Q.; Zan, L.; Tian, L. H.; Peng, T. Y.; Zhang, J. J. *Chem. Commun.* **2011**, *47*, 6951.
(20) Jiang, J.; Zhao, K.; Xiao, X. Y.; Zhang, L. Z. *J. Am. Chem. Soc.* **2012**, *134*, 4473.
(21) Hahn, N. T.; Hoang, S.; Self, J. L.; Mullins, C. B. *ACS Nano* **2012**, *6*, 77122.
(22) Xiong, J. Y.; Cheng, G.; Li, G. F.; Qin, F.; Chen, R. *RSC Adv.* **2011**, *1*, 1542.
(23) Robles, J. M. C.; Ogando, E.; Plazaola, F. *J. Phys.: Condens. Matter* **2007**, *19*, 176222.
(24) Barbiellini, B.; Puska, M. J.; Korhonen, T.; Harju, A.; Torsti, T.; Nieminen, R. M. *Phys. Rev. B* **1996**, *53*, 16201.
(25) Zhao, J. C.; Wu, T. X.; Wu, K. Q.; Oikawa, K.; Hidaka, H.; Serpone, N. *Environ. Sci. Technol.* **1998**, *32*, 2394.
(26) Wu, T. X.; Liu, G. M.; Zhao, J. C.; Hidaka, H.; Serpone, N. *J. Phys. Chem. B.* **1998**, *102*, 5845.
(27) Liu, X. W.; Zhou, K. B.; Wang, L.; Wang, B. Y.; Li, Y. D. *J. Am. Chem. Soc.* **2009**, *131*, 3140.
(28) Xiao, C.; Qin, X. M.; Zhang, J.; An, R.; Xu, J.; Li, K.; Cao, B. X.; Yang, J. L.; Ye, B. J.; Xie, Y. *J. Am. Chem. Soc.* **2012**, *134*, 18460.
(29) Liu, G.; Niu, P.; Sun, C. H.; Smith, S. C.; Chen, Z. G.; Lu, G. Q.; Cheng, H. M. *J. Am. Chem. Soc.* **2010**, *132*, 11642.

NOTE ADDED AFTER ASAP PUBLICATION

References 22 and 23 were transposed in the version published asap on July 3, 2013; the correct version reposted on July 5, 2013.